Supplementary information

Halide perovskites enable polaritonic *XY* spin Hamiltonian at room temperature

In the format provided by the authors and unedited

Supplementary Information for

Halide perovskites enable polaritonic XY spin Hamiltonian at room temperature

Renjie Tao[1]*, Kai Peng[2]*, Louis Haeberlé[3], Quanwei Li[4], Dafei Jin[5], Graham R. Fleming[4], Stéphane Kéna-Cohen[3], Xiang Zhang[1,6]†, and Wei Bao[2]†

*These authors contributed equally to this work.
†Corresponding author. Email: wbao@unl.edu or xiang@berkeley.edu

[1]Nanoscale Science and Engineering Center, University of California, Berkeley, California, United States

[2]Department of Electrical and Computer Engineering, University of Nebraska-Lincoln, Lincoln, Nebraska, United States

[3]Department of Engineering Physics, École Polytechnique de Montréal, Montréal, Quebec, Canada

[4]Department of Chemistry, University of California, Berkeley, California, United States

[5]Center for Nanoscale Materials, Argonne National Laboratory, Lemont, Illinois, United States

[6]Faculty of Science and Faculty of Engineering, The University of Hong Kong, Hong Kong, China

This PDF file includes:

Supplementary Text
Supplementary Figs. 1 to 27

Supplementary Text

Section I: Polariton model

The photon-exciton strong coupling can be described using a coupled oscillator model neglecting linewidths:

$$\begin{pmatrix} E_{cav}(k) & \Omega/2 \\ \Omega/2 & E_{ex} \end{pmatrix} \begin{pmatrix} a \\ b \end{pmatrix} = E \begin{pmatrix} a \\ b \end{pmatrix}.$$

Here, the cavity mode is represented as $E_{cav}(k) = E_0 + \dfrac{\hbar^2 k^2}{2m}$ with cutoff photon energy E_0 and effective mass m. E_{ex} is the exciton energy of the perovskites. Ω is the Rabi splitting. E is the eigenvalue of the polaritons, and a and b represent the Hopfield coefficients satisfying $|a|^2 + |b|^2 = 1$.

Meanwhile, the spin-orbit coupling induces TE-TM mode splitting of the planar microcavity, which have two polarized modes with different effect masses m_{TE} and m_{TM}. The material birefringence in the cavity breaks the cylindrical symmetry of TE and TM modes and lifts their degeneracy at k = 0. This spin-orbit coupling can be described on a circular polarization basis with parabolic approximation as [1,2]:

$$H_k = \begin{pmatrix} E_0 + \dfrac{\hbar^2 k^2}{2m} & \alpha - \beta k^2 e^{-2i\varphi} \\ \alpha - \beta k^2 e^{2i\varphi} & E_0 + \dfrac{\hbar^2 k^2}{2m} \end{pmatrix}$$

where $m = m_{TE} m_{TM}/(m_{TE} + m_{TM})$ is the reduced effective mass; $k = |k_\parallel| = \sqrt{k_x^2 + k_y^2}$ is the in-plane wavevector ($k_x = k\cos\varphi$, $k_y = k\sin\varphi$, φ is the propagation angle). α and β represent the optical birefringence from anisotropy and TE-TM splitting from spin-orbital coupling, respectively. Along y-direction ($\varphi = \pi/2$), the two polariton branches cross at $k_y = \pm\sqrt{\alpha/\beta}$, as two diabolical points. With consideration of the strong coupling with the exciton, the Hamiltonian can be written as:

$$H_k = \begin{pmatrix} E_0 + \dfrac{\hbar^2 k^2}{2m} & \dfrac{\Omega}{2} & \alpha - \beta k^2 e^{-2i\varphi} & 0 \\ \dfrac{\Omega}{2} & E_{ex} & 0 & 0 \\ \alpha - \beta k^2 e^{2i\varphi} & 0 & E_0 + \dfrac{\hbar^2 k^2}{2m} & \dfrac{\Omega}{2} \\ 0 & 0 & \dfrac{\Omega}{2} & E_{ex} \end{pmatrix}$$

The two lower polariton branches in Fig 1g along x and y-axis was fitted well with this model. The Hopfield coefficients can be obtained by calculating the eigenvectors. Here, exciton energy was extracted from the absorption spectrum as E_{ex} = 2406 meV. Other parameters in the

Hamiltonian were fitted with small uncertainties as E_0 = 2336.43±7.78 meV, m = 0.12 ±0.01 meV/(μm/(ps))^2, α = 6.21 ±0.41 meV, β = 0.18 ±0.01 meV μm^2, Ω = 138.16±12.54 meV. Along y-direction in Fig 1g, the two branches cross at k_y = 5.9 μm^{-1}. Another set of polariton dispersions with different detuning was also fitted with consistent parameters as shown in Fig. S21.
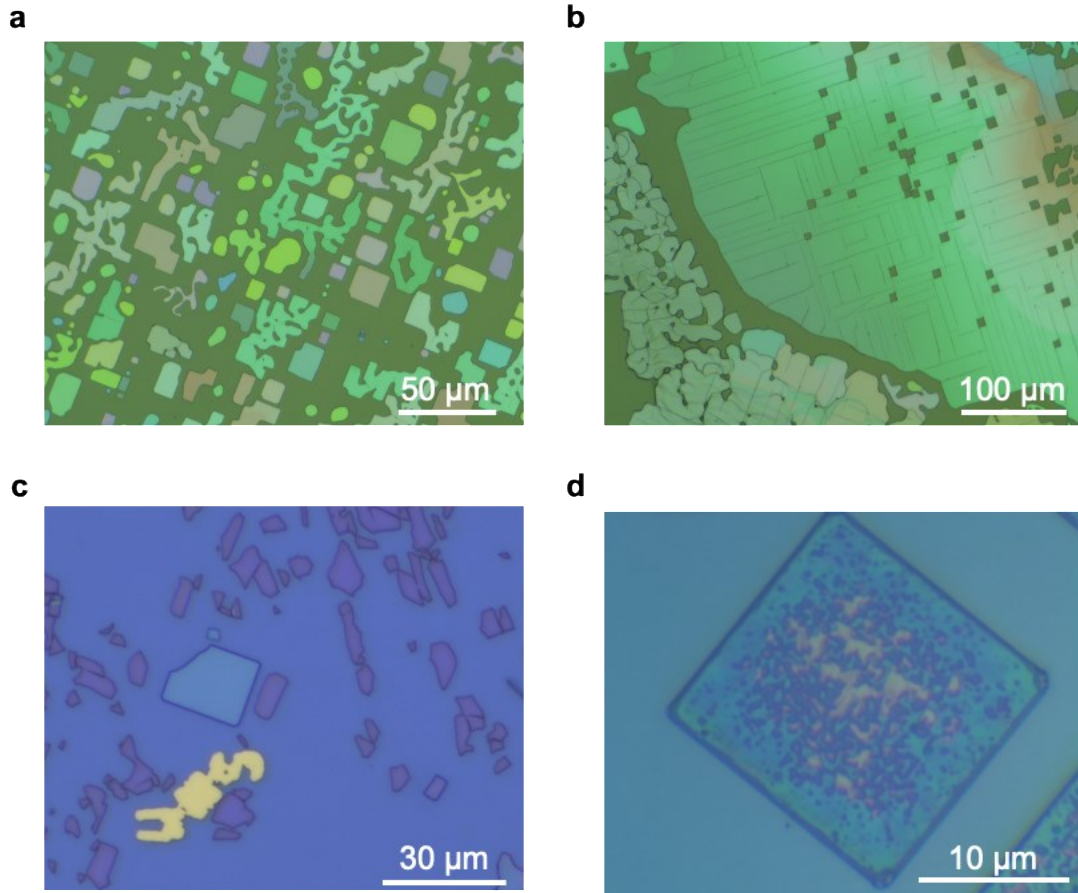
Supplementary Fig. 1 | Typical problems with convention perovskite samples. While spin-coating and other solution bulk crystal growth methods cannot produce thin perovskite samples with homogenous and reliably pronounced exciton properties, CVD growth method is so far the only way for perovskite polaritonics. However, several serious problems are associated with CVD perovskite samples. First, crystal thickness is random and uncontrolled as evidenced by the various crystal colors (**a**), but only specific one is desired to achieve strong coupling of excitons and photons with the right cavity detuning. Second, only small lateral sized crystals (~ 20 μm) are achieved since there is no strongly preferred growth directions of halide perovskites. This small crystal size prohibits the room temperature quantum simulation of many important phenomena. Larger crystals are too thick and with cracks and holes (**b**) due to strain relaxation. Third, due to the brittle nature of the ionic halide perovskite crystals, the transfer of them on to DBR substrates easily leads to broken pieces (**c**). Four, the following high-temperature deposition of high-quality top DBR to form the optical cavity will introduce damage to the crystals (**d**). Stress of the DBR films and poor adhesion of the perovskite crystal to the substrate also limit the thickness top DBR mirrors, and hence the optical quality. In contrast, our strategy is to directly synthesize crystals in the prefabricated nanocavities, after which, the crystals are already sandwiched by the two DBR mirrors, free from possible damages caused by mechanical transfer or top DBR depositions. Our method decouples the DBR fabrications with the integration of halide perovskite materials so that one does not need to sacrifice the optical quality of the DBR mirrors for the protection of halide perovskite materials at all.

4
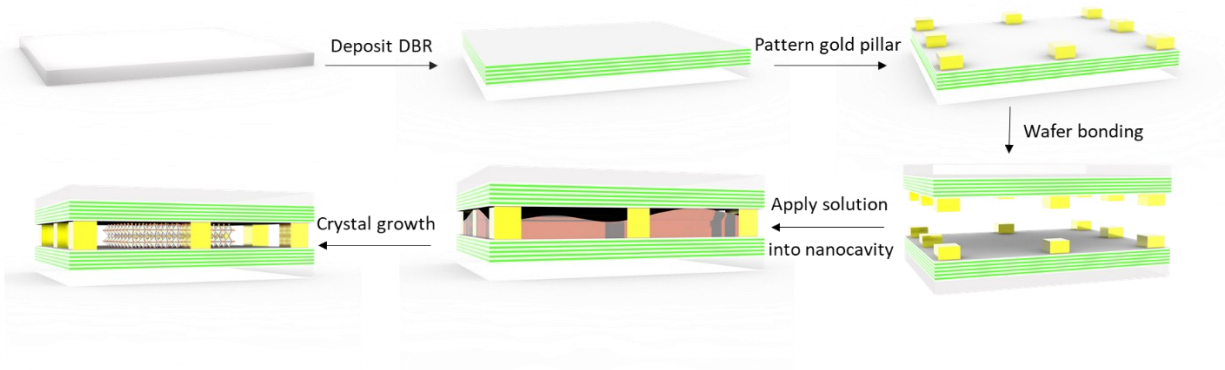
Supplementary Fig. 2 | Schematics of solution-based crystal synthesis in nanocavities. By utilizing electron-beam deposited gold pillar arrays of a specific height as spacers and bonders in between two DBR mirrors (nine pairs of SiO_2 and Ta_2O_5 alternating layers), a nanocavity of a designed height for halide perovskite crystals to grow in is formed so that the detuning between exciton and photon can be tuned for the strong coupling.
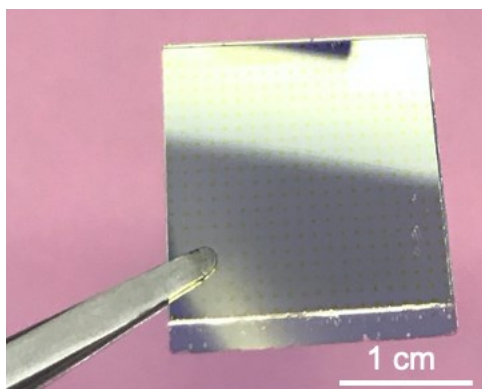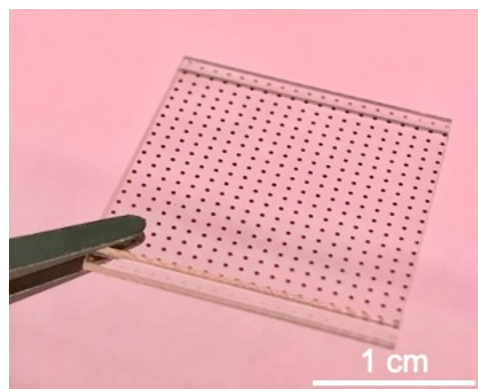
Supplementary Fig. 3 | Images of fabricated chips. **a,** Bonded DBR wafers were diced into small (2 cm × 2 cm) chips for crystal growth. **b,** Bonded quartz wafers without DBR mirrors is for a better visualization of the gold pillar arrays.
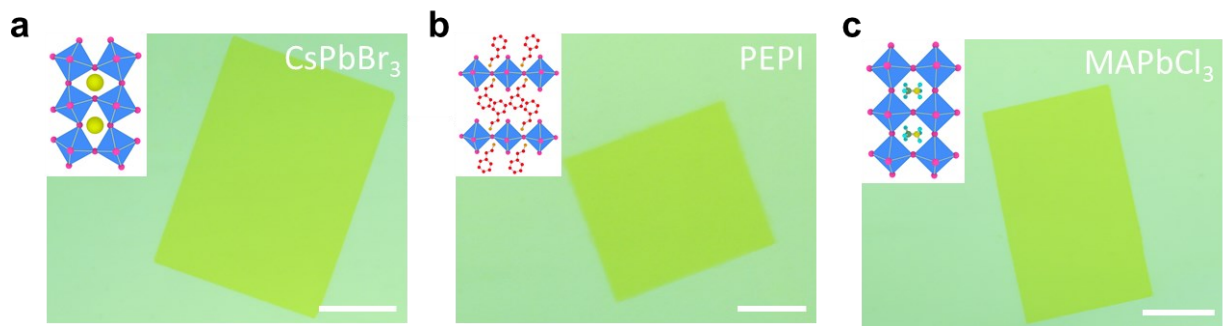
Supplementary Fig. 4 | Optical images of halide perovskite crystals grown in nanocavities. Various excitonic halide perovskite single crystals can be grown in the nanocavities, and large sizes of ~ 300 μm are shown. The chemical compositions of the perovskite crystals in the figure are all-inorganic bromide perovskite $CsPbBr_3$ (**a**), 2D layered iodide perovskite $(C_6H_5C_2H_4NH_3)_2PbI_4$ (PEPI) (**b**), and organic-inorganic hybrid chloride perovskite $MAPbCl_3$ (**c**). Scale bars in **a-c**, 100 μm. The after-growth cavity can also be opened without damaging the crystals for patterning purposes if needed.
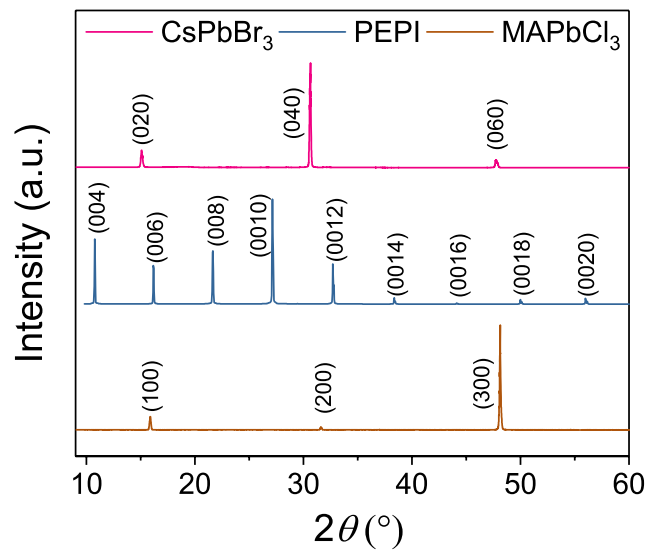
Supplementary Fig. 5 | X-ray diffraction characterization of the as-grown single crystals in Supplementary Fig. 4. The sharp peaks suggest high crystallinity of the samples.
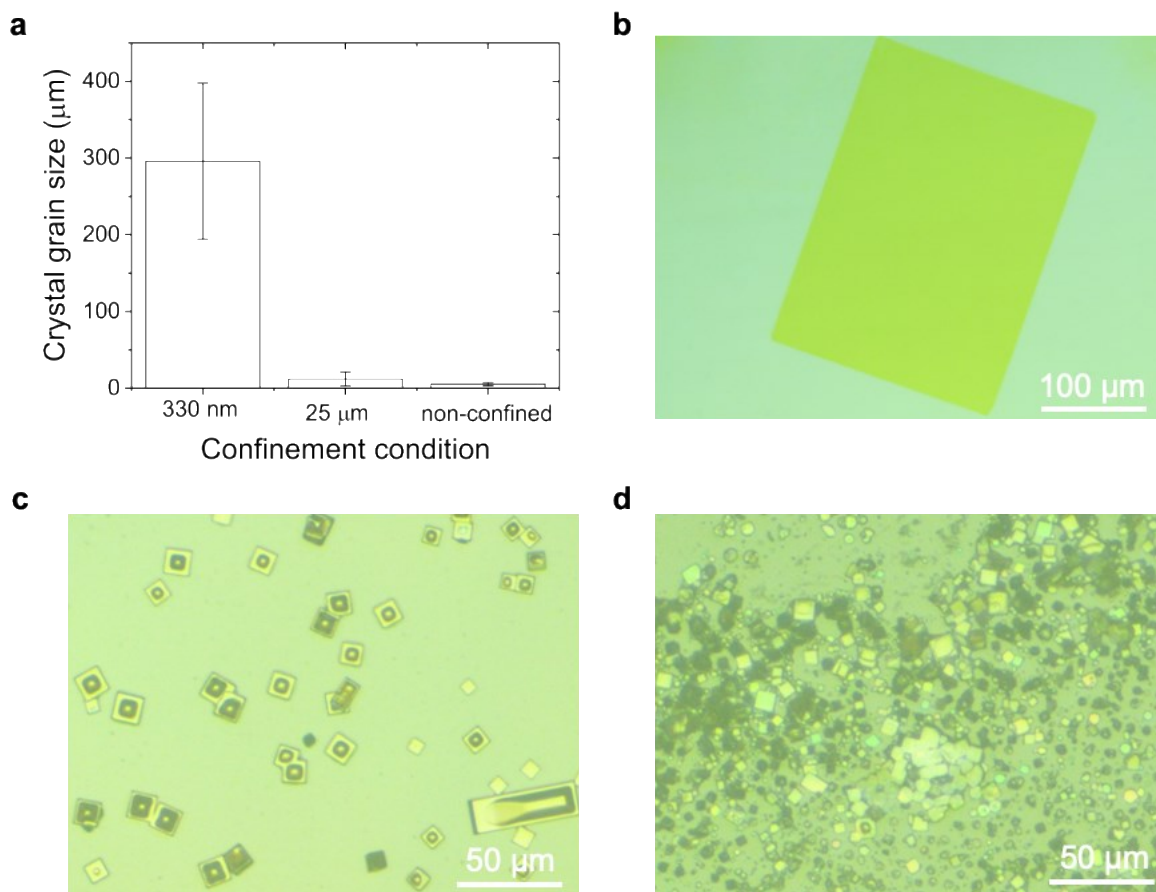
Supplementary Fig. 6 | Optical images of halide perovskite crystal grown under different confinement conditions. **a,** $CsPbBr_3$ crystals showed average sizes of ~300 µm, 12 µm, and 5 µm when in 330 nm height nanocavities (**b**), 25 µm thick channels (**c**), and without any confinement (**d**), respectively. This indicates that a confined environment results in a larger crystal size. 25-µm thick channels were fabricated by bonding two glass wafers together with 25 µm thick double-sided tape. Non-confined synthesis was conducted by dropping solutions directly on a quartz wafer. All other synthesis conditions were the same as described in the Materials and Methods section.
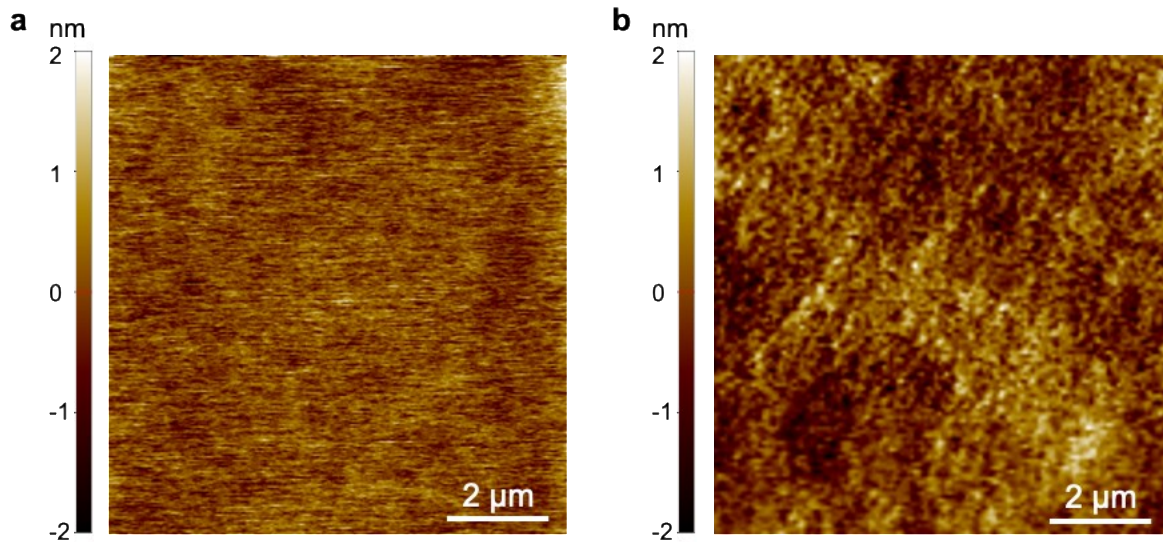
Supplementary Fig. 7 | AFM images of deposited DBR mirror surfaces and CsPbBr$_3$ crystal surfaces synthesized from nanocavity. **a,** An AFM image shows the root mean square (r.m.s.) roughness of the DBR mirrors' surface of ~ 0.4 nm within 100 μm^2, indicating an advanced plasma source improves DBR layers' surface roughness, hence reducing the interface scattering and enhancing the optical quality of DBR mirrors. **b,** Grown in between ultra-flat DBR mirror nanocavities, halide perovskite crystal shows a surface r.m.s. roughness of only 0.5 nm over 100 μm^2, which was only 2% of the film grown by traditional spin-coating methods [3], and was comparable with the CVD grown sample [4].
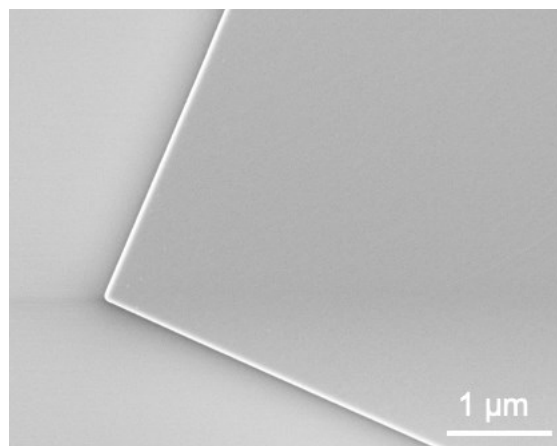
Supplementary Fig. 8 | SEM image of a halide perovskite crystal. The SEM image shows a uniform and featureless surface of the synthesized CsPbBr$_3$ crystal from nanocavities.
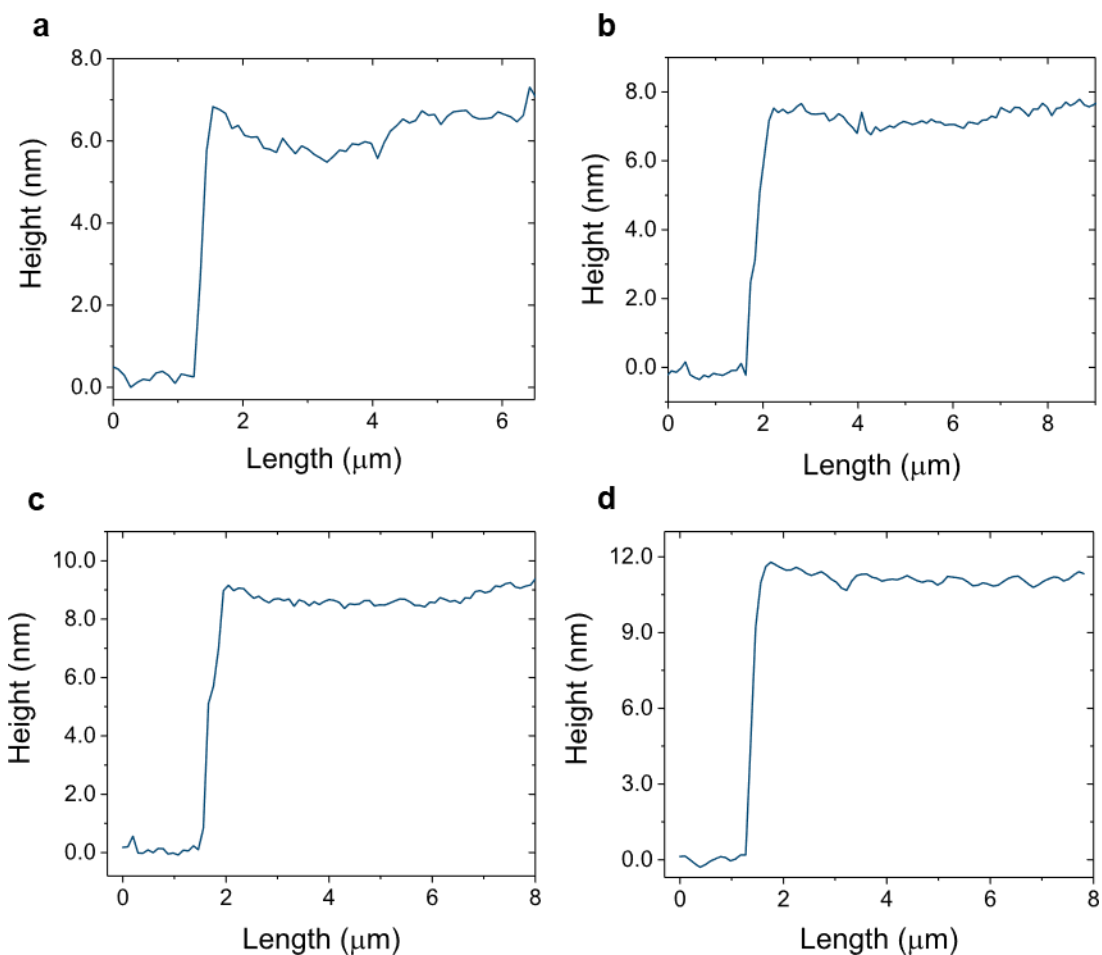
Supplementary Fig. 9 | Height profiles of ultra-thin crystals grown from nanocavities. When shrinking down the thickness of the cavities, the synthesized halide perovskite crystals from these nanocavities show only a few nanometers thickness (**a-d** and Fig. 1**e**). Such ultra-thin crystals experience strong blue shifts of photoluminescence (Fig. 1**e**) due to the quantum confinement effect. This will provide a degree of freedom to control over the excitonic energy level.
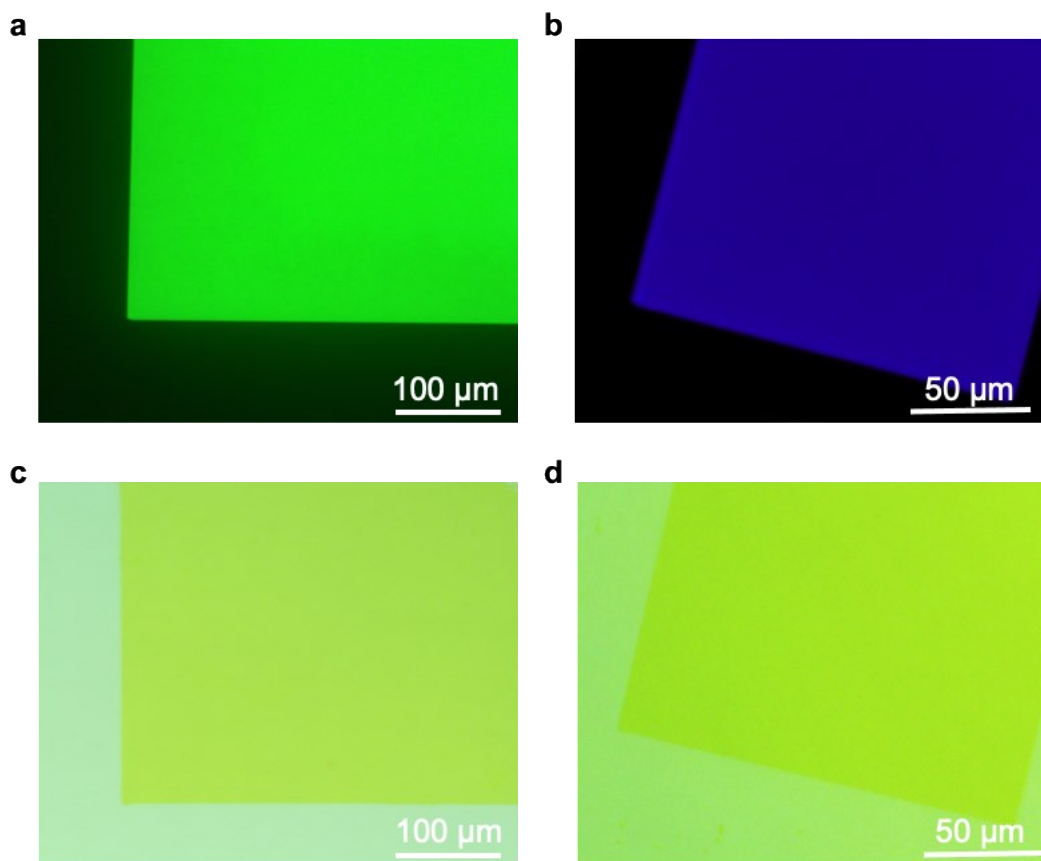
Supplementary Fig. 10 | Bright and uniform PL of halide perovskite over an area of hundreds of microns, synthesized from nanocavities. Fluorescence microscopy images of 2D layered halide perovskite PEPI (**a**) and organic-inorganic hybrid halide perovskite MAPbCl$_3$ (**b**) under ultraviolet excitation and their corresponding optical microscopy images (**c-d**).
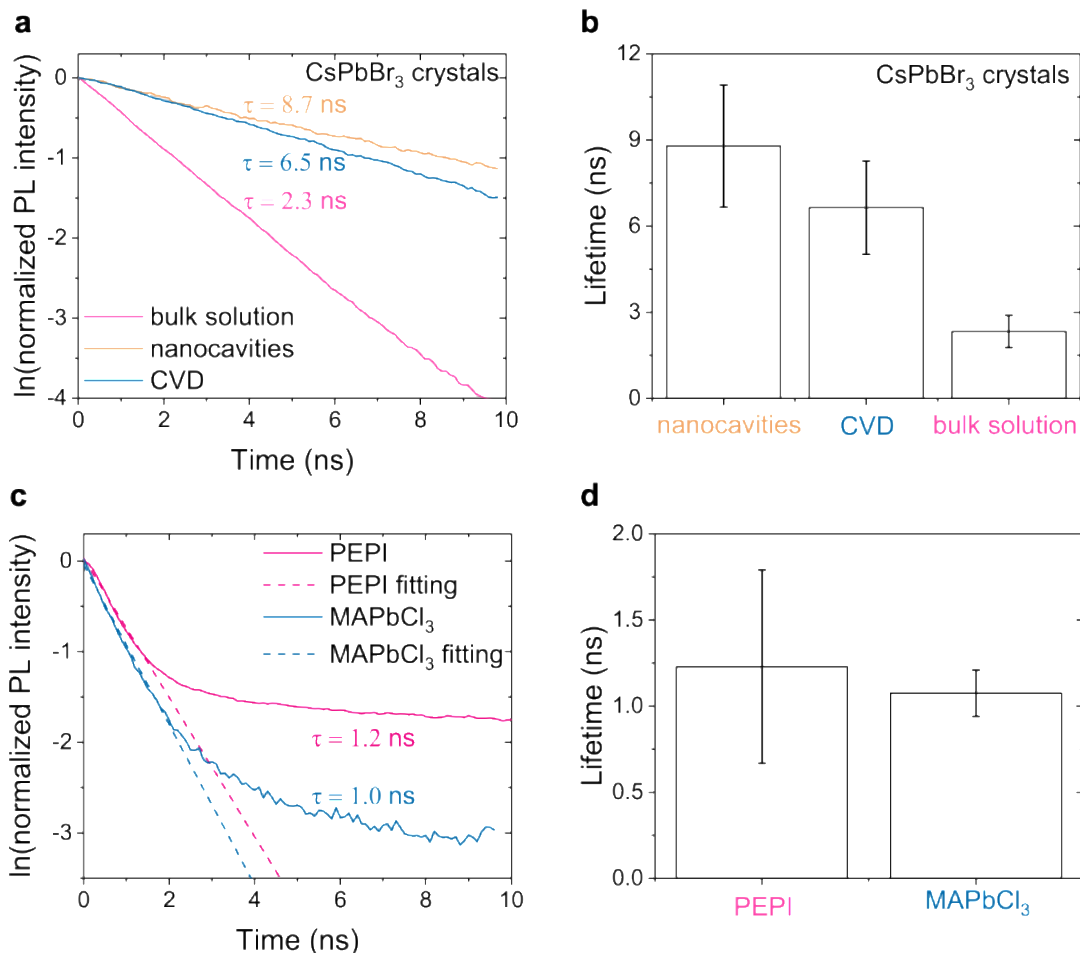
Supplementary Fig. 11 | Various excitonic halide perovskites PL lifetimes and their statistics. **a** and **b** are the PL lifetimes and statistics of $CsPbBr_3$ synthesized by different methods. The solution-synthesized $CsPbBr_3$ crystals from nanocavities show an average lifetime of 8.7 ns, comparable to the $CsPbBr_3$ nanoplates, 6.5 ns, synthesized by the high-temperature epitaxial CVD method, and far longer than crystals synthesized from bulk solution (2.3 ns). This long PL lifetime implies superior crystal quality from the nanocavity. **c** and **d** are the PL lifetimes and their statistics of PEPI and $MAPbCl_3$ from nanocavities showed an appreciably long PL lifetime.
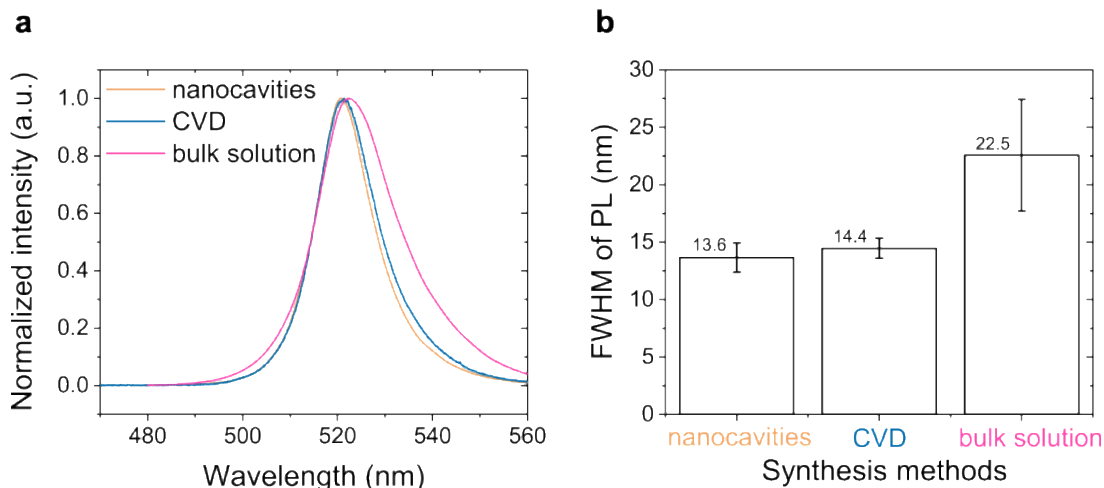
Supplementary Fig. 12 | PL full width at half maximum (FWHM) of $CsPbBr_3$ single crystals synthesized by different methods. The low temperature solution-synthesized $CsPbBr_3$ crystals from nanocavities showed a narrow emission peak with an FWHM of only 13.6 nm (yellow curve, **a**) at room temperature, which is comparable to the $CsPbBr_3$ nanoplates synthesized by the high-temperature epitaxial CVD method (blue curve, **a**) and far narrower than crystals synthesized from a bulk solution (22.5 nm) (magenta curve, **a**) similar as in ref. [5], statistics are in **b**. This narrow FWHM implies superior homogenous crystal quality of the nanocavity-grown samples.
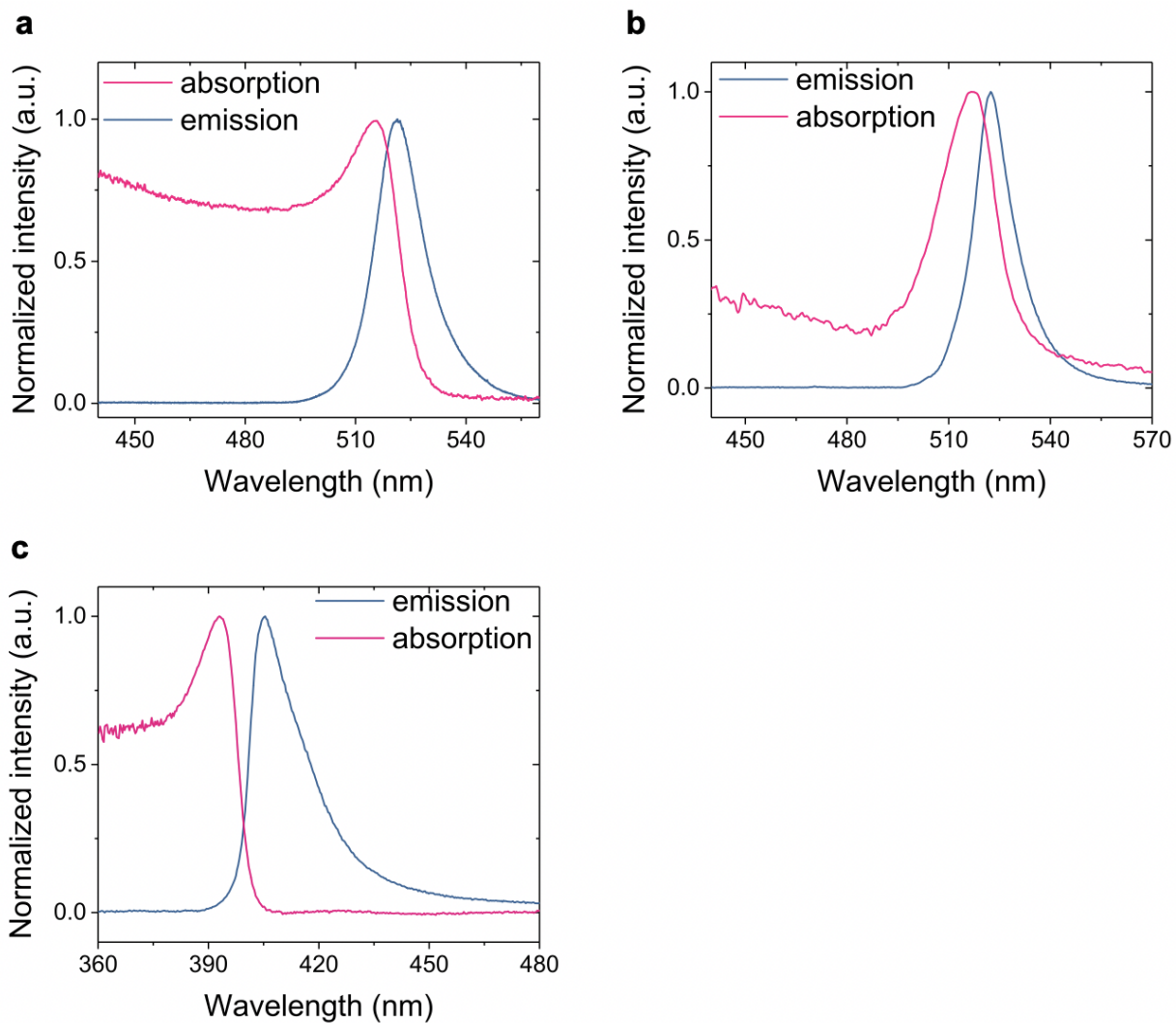
Supplementary Fig. 13 | Room-temperature absorption and emission spectra of all-inorganic halide perovskite CsPbBr$_3$ (**a**), 2D layered halide perovskite PEPI (**b**), and organic-inorganic hybrid perovskite MAPbCl$_3$ (**c**). All samples synthesized from nanocavities showed strong and stable excitonic absorption peaks at room temperature, indicating their potential for room-temperature polaritonic applications. Their corresponding emission peaks were at 515, 522, and 405 nm, respectively.
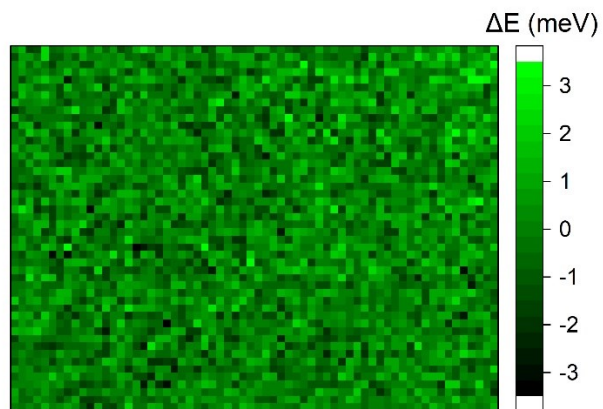
Supplementary Fig. 14 | PL mapping of the lower polariton branch. The scanning step is 1 μm. Here, the energy fluctuation of the sample within 48×64 μm^2 is within ±3.4 meV, demonstrating the superb homogeneity of the synthesized perovskite crystals from nanocavities. The root-mean-square variation value is 1.02 meV.
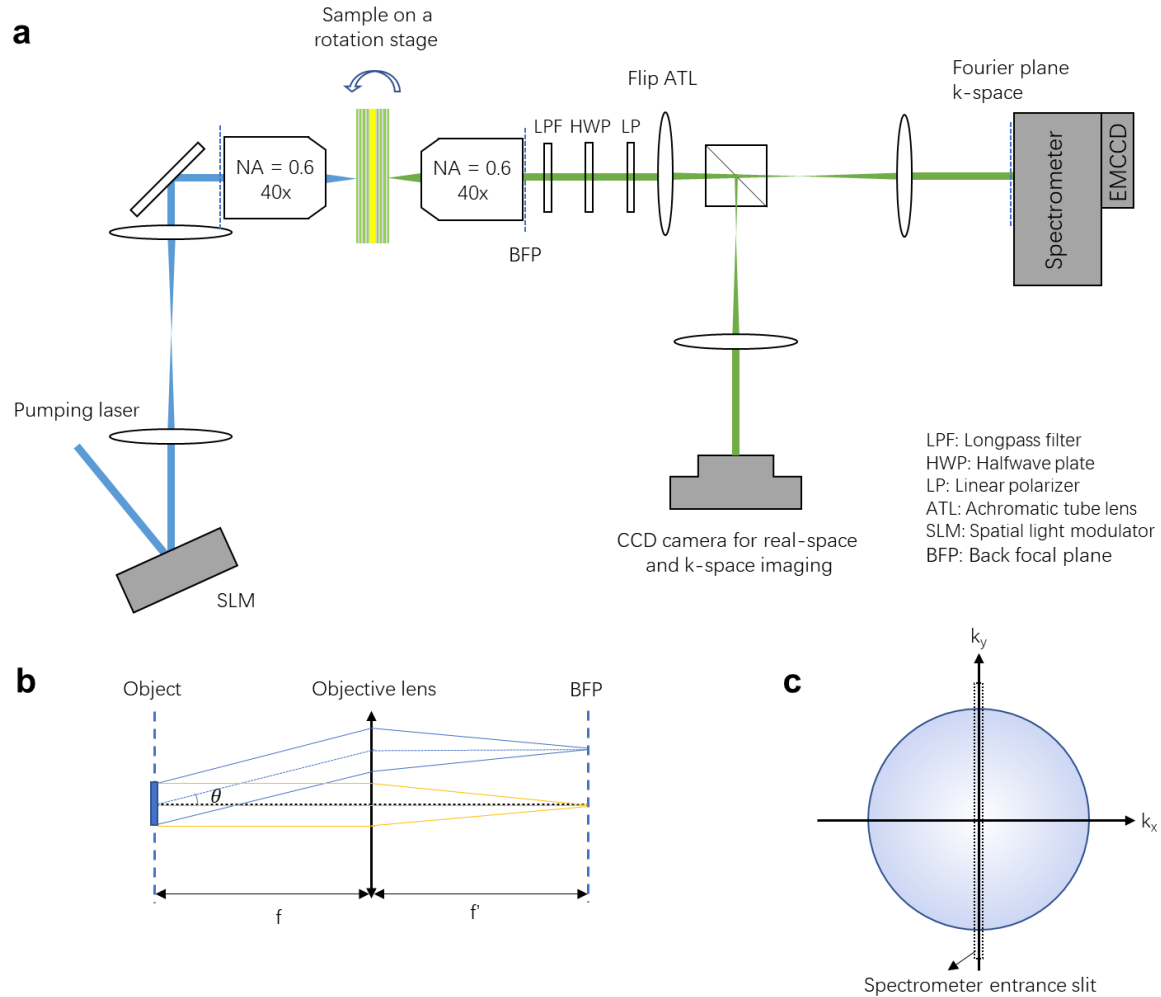
Supplementary Fig. 15 | Schematics of the optical measurements setup. a. Experimental setup for room-temperature polaritonic XY Hamiltonians simulation. A reflective liquid-crystal phase-only spatial light modulator (SLM) is used to generate non-resonant excitation laser patterns at the focal plane of a Nikon 40x objective. The PL was collected in a transmission configuration. The k-space images can be obtained by a Fourier imaging configuration with two achromatic tube lenses. An Andor spectrometer equipped with an EMCCD was used to measure the energy-resolved polariton dispersions. A CCD camera was used to obtain 2D k-space images and the real-space images by flipping the first achromatic tube lens. A long-pass filter was used to filter the excitation laser. The linear-polarized PL dispersions can be obtained with a halfwave plate and a linear polarizer. **b**. The schematic of the back focal plane (BFP) of an objective lens. Here the focal lengths before and after the objective lens are marked as f and f'. The rays emitted from the object to the same angular orientation lie onto the same lateral coordinate at the BFP, as the blue and orange lines are shown. Therefore, each point in the BFP is the superimposition of the photon field emitted by the source along a given direction. This Fourier plane is projected onto the spectrometer entrance plane via two imaging lenses and finally imaged through the narrow entrance slit of the spectrometer and dispersed onto the 2D EMCCD array. The slit transmits one line along the diameter of the Fourier plane; each point of this line can represent the emission angle θ, as shown in **c**. The Fourier plane can also be projected to a CCD camera to achieve 2D k-space imaging. A

18

rotation stage is used to rotate the sample to obtain the dispersions along the x and y-axis in Fig. 1**g** and Supplementary Fig. 21. A halfwave plate and a linear polarizer were used to measure the polarization.
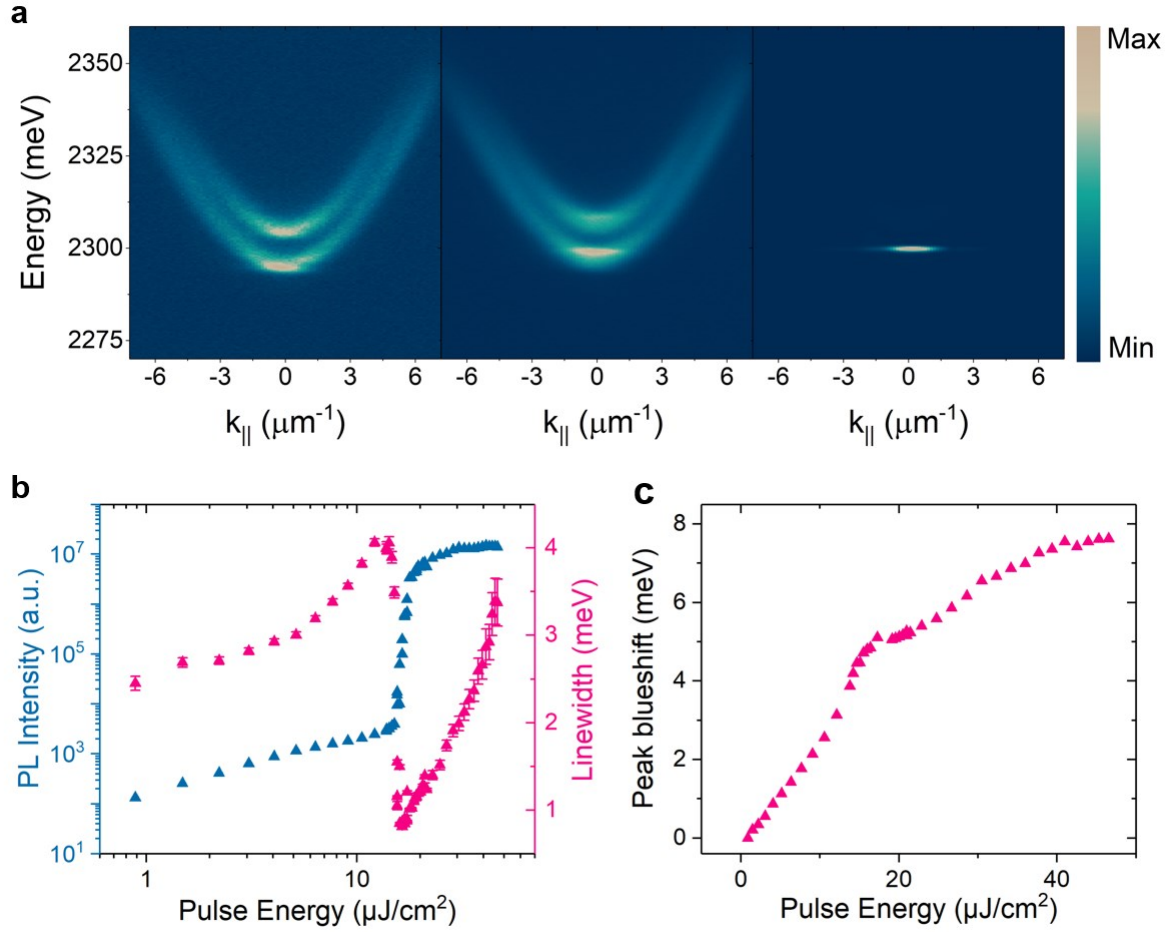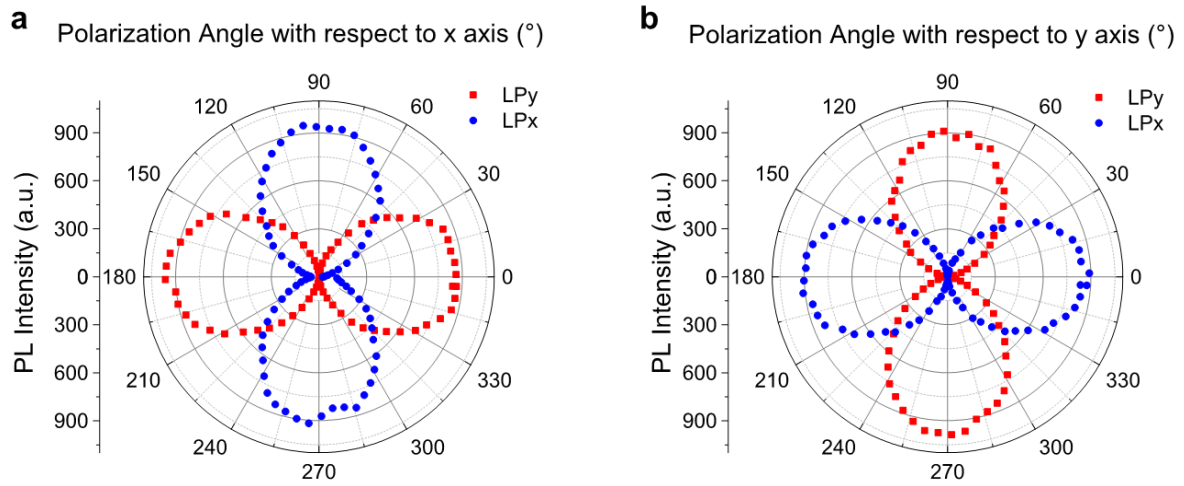
Supplementary Fig. 16 | Exciton-polariton condensation under non-resonant excitation at room temperature. The pumping laser spot size is ~15 μm. **a,** The k-space power-dependent angle-resolved PL spectra at 0.22 P_{th}, P_{th}, and 1.2 P_{th}, where P_{th} (~ 13 μJ cm^2) is the pumping power of condensation threshold. With the power increasing, the ground state of the mode along the **x**-axis at $k_{||}$ = 0 condensates. **b,** Log-log plot of integrated PL intensity of LP_x at $k_{||}$ = 0 and FWHM of LP_a versus pumping power. The collapse in k-space, nonlinear increasing of PL intensity, and narrowing of linewidth clearly show polariton condensation behavior. **c,** PL peak blueshift of LP_x at $k_{||}$ = 0 versus pumping power. A strong blueshift was observed below the threshold due to the strong excitonic interactions.
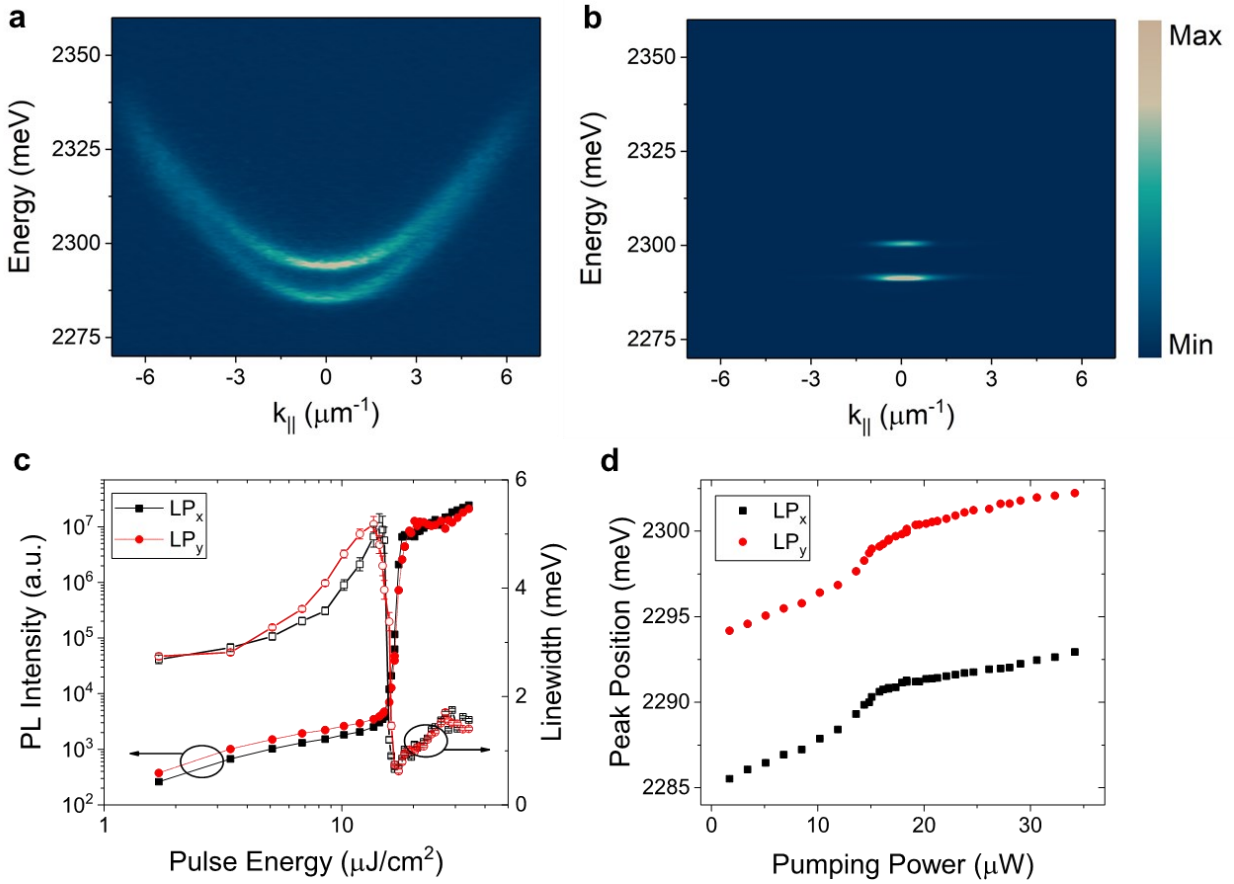
Supplementary Fig. 17 | Exciton-polariton condensation under non-resonant excitation at room temperature. The pumping laser spot size is ~15 μm. Here, condensations can be observed in both two lower branches. Due to the different detuning induced different gain and loss. **a,** The k-space power-dependent angle-resolved PL spectra at 0.12 P_{th} and 1.29 P_{th}, where P_{th} (~ 15 μJ cm^2) is the pumping power of condensation threshold. With the power increasing, the ground states of the mode along x-axis and y-axis at $k_{\parallel} = 0$ condensate. **b,** Log-log plot of integrated PL intensities of LP_x and LP_y at $k_{\parallel} = 0$ and FWHMs of LP_x and LP_y versus pumping power. **c,** PL peak blueshifts of LP_x and LP_y at $k_{\parallel} = 0$ versus pumping power.
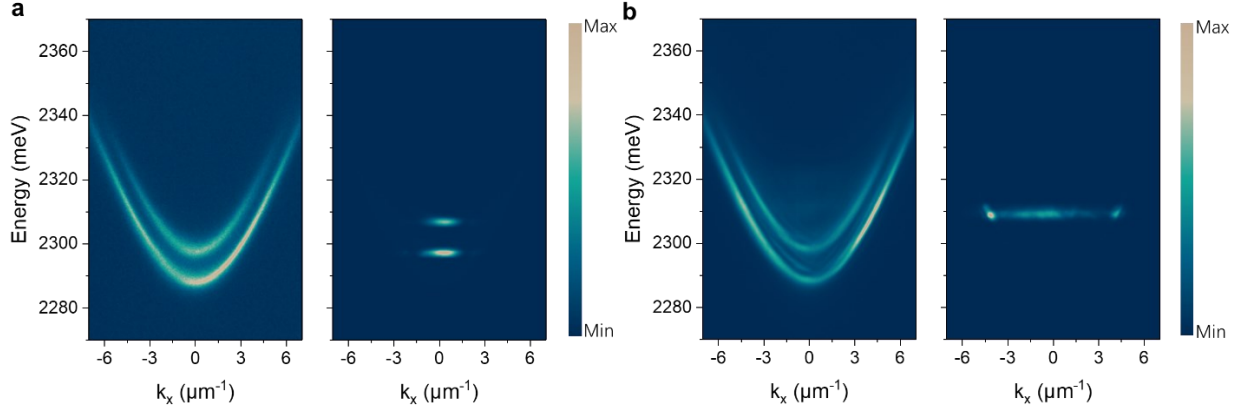
Supplementary Fig. 18 | Polariton condensations under non-resonant excitations with large and small laser spot sizes at the same position of the sample. The laser spot size can be tuned easily by adjusting the focus of the objective in the excitation path. **a**. The k-space dispersions before and after condensation (~1.3 P_{th}) with a pumping laser spot of ~15 μm (Gaussian FWHM). The two lower polariton branches condensate near $k_x = 0$. **b**. The k-space dispersions before and after condensation (~1.3 P_{th}) with a pumping laser spot of ~1.5 μm (Gaussian FWHM). The lower polariton branch along *x*-axis condensates at $k_x = 4.1$ μm^{-1}. According to the theoretical model [6], the non-resonant excitation generates an exciton reservoir to provide polaritons for the condensate. Meanwhile, the repulsive interactions between polaritons also create a repulsive potential to ballistic accelerate the polaritons with a nonzero momentum. Therefore, a broadening of the condensate momentum distribution can be observed with a large laser spot in **a**. When the pumping laser spot is much smaller than the characteristic propagation length, most of the polaritons will ballistically propagate outside the excitation region with a finite in-plane wavevector, as shown in **b** with a small laser spot.

Supplementary Fig. 19 | The polarization dependence of polariton emissions at k = 0 observed along *y* and *x*-axis. **a** and **b** are measured along $k_y = 0$ and $k_x = 0$ from the left and the right panel in Fig 1**g**, respectively. The linear polarization of the two branches can be observed clearly.
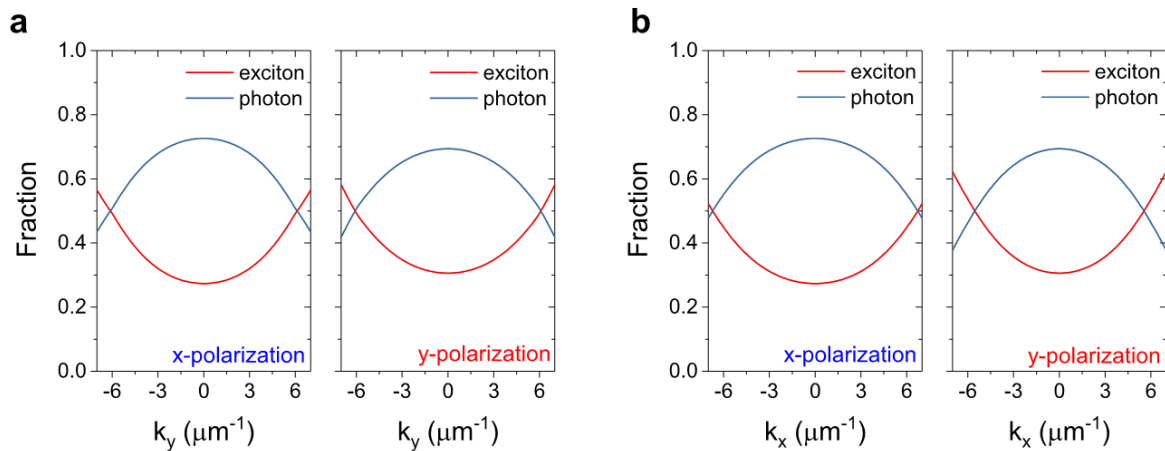
Supplementary Fig. 20 | The Hopfield coefficients of lower polariton branches along *y* and *x*-axis. **a** and **b** are the fitting results of the left and right panels of Fig 1**g**, respectively. Based on the coupled oscillator model combining spin-orbital coupling in Section I, the exciton and photon components in polariton states as a function of in-plane momentum can be characterized.
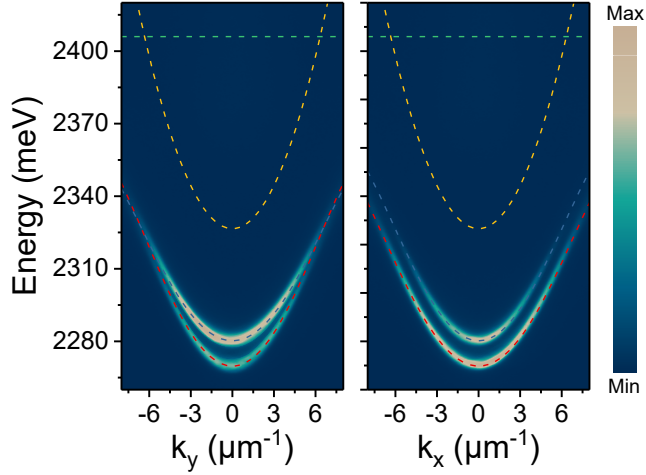
Supplementary Fig. 21 | Angle-resolved PL of CsPbBr₃ polariton dispersions along *y* and *x*-axis with a different detuning. Here, exciton energy was extracted from the absorption spectrum as E_{ex} = 2406 meV. Other parameters in the Hamiltonian were fitted as E_0 = 2326.56±5.1 meV, m = 0.11±0.01 meV/(μm/(ps))^2, α = 7.3±0.29 meV, β = 0.17±0.01 meV μm^2, Ω = 164.28±8.14 meV. Along y-direction in the left panel, the two branches cross at k_y = 6.65 μm^{-1}.
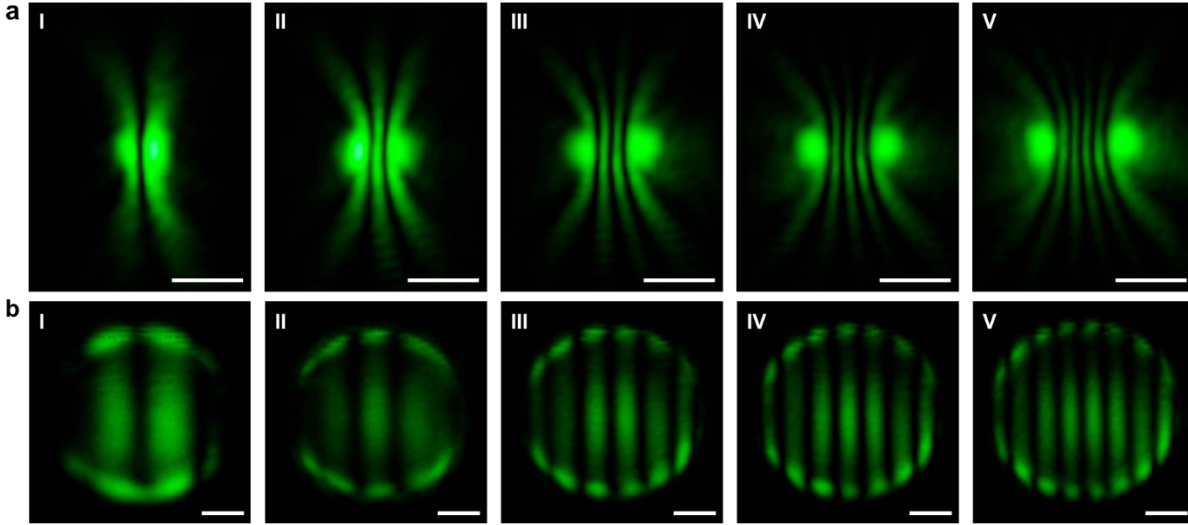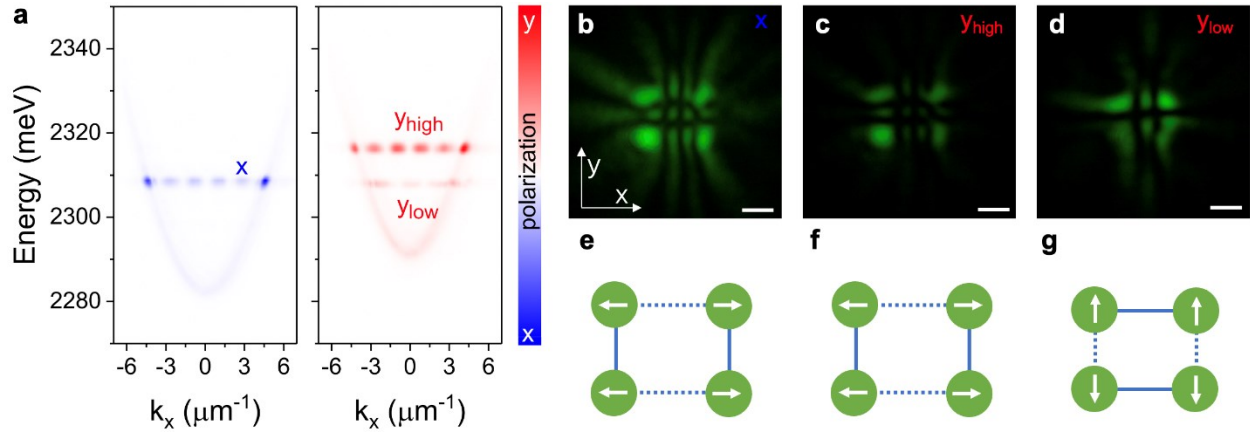
Supplementary Fig. 22 | Phase configurations of a polariton dyad with different separation distances between two condensates. a-I-V. The time-integrated real-space images of a polariton dyad with different separation distances (I-V: 2.4, 3.9, 4.34, 4.82, 5.3 μm). **b**-I-V, The time-integrated k-space images correspond to **a**-I-V. The polariton condensates at ~4.1 μm^{-1}. By tuning the distances of the two polariton condensates, the numbers of interference fringes between the two condensates oscillate from zero or even to odd periodically, revealing the antiphase to the in-phase synchronization. The pumping laser spot size is ~1.5 μm. Scale bars in **a**, 5 μm. Scale bars in **b**, 2 μm^{-1}.
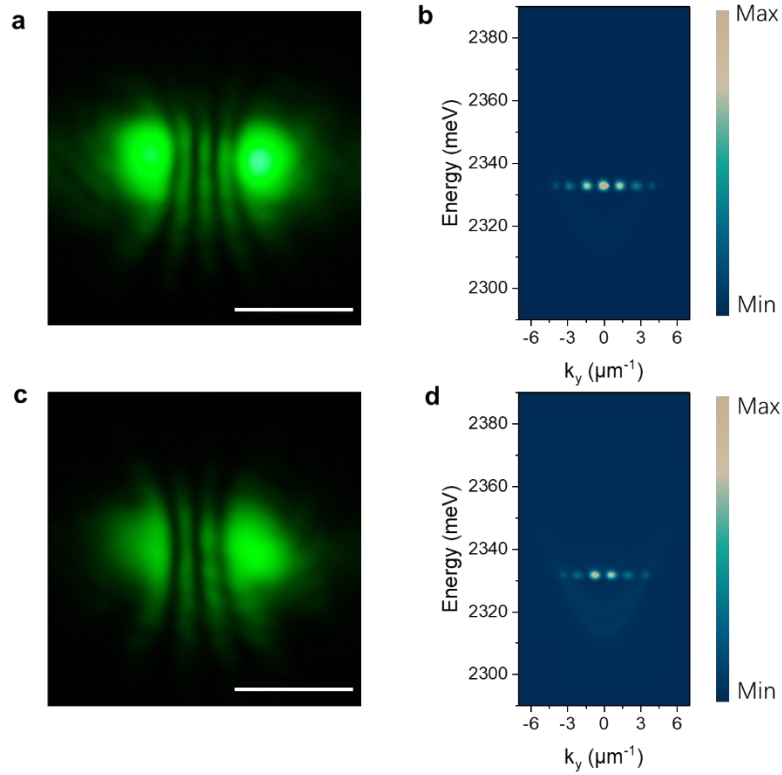
Supplementary Fig. 23 | Phase configurations of a polariton dyad with different pumping laser spot sizes. The real-space image (**a**) and *k*-space dispersion (**b**) of a polariton dyad with a pumping laser spot size of ~1.5 μm. The lower polariton branch along the *y*-axis condensates at $k_y = 4\,\mu m^{-1}$. The in-phase ferromagnetic configuration can be observed by the odd interference fringes between two condensates. With a larger laser spot size of ~1.75 μm in **c** and **d**, the polaritons condensates at $k_y = 3.4\,\mu m^{-1}$. The phase difference between two condensates becomes π, as the even interference fringes are shown in **c** and **d**. Scale bars in **a** and **c**, 5 μm. The laser spot sizes were tuned by the SLM directly with the distance between the two spots unchanged.
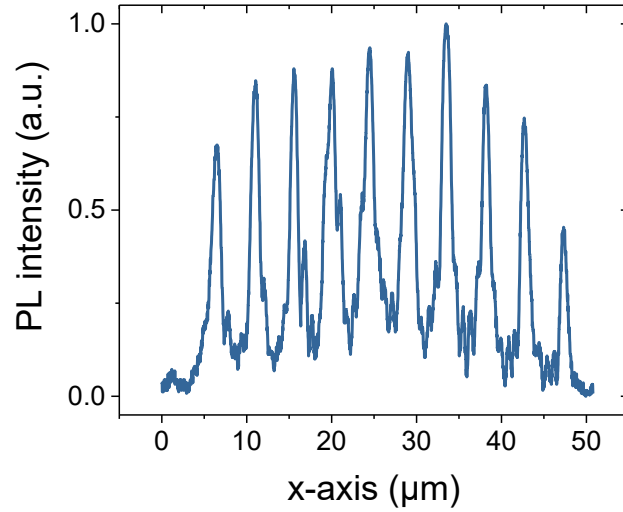
Supplementary Fig. 24 | A typical normalized line profile of a polariton chain extracted from the 10×10 polariton lattice in Fig. 3c with anti-ferromagnetic coupling. Due to the polariton outflow, the intensities of the nodes at the boundary are lower, revealing a deviation of the π phase differences[7,8]. To accurately extract the phase difference, especially for this complex geometry, one must use sophisticated interferometry in k-space.

Supplementary Fig. 25 | Room-temperature demonstration of polariton XY Hamiltonian in 90° compass configuration. An excitation pattern in a 2×2 rectangle configuration is applied. **a**, Time-integrated k-space polariton dispersion along x axis. At the branch with x polarization (left panel), the condensation occurs at 4.5 μm⁻¹. The even number of interference fringe along x axis in the corresponding real-space image (**b**) shows an anti-phase coupling. At the branch with y polarization (right panel), the condensation occurs at two wave vectors (y_{high}: $k_c = 4.2$ μm⁻¹, y_{low}: $k_c = 3.3$ μm⁻¹.). **c** and **d** are the time-integrated real-space images or y_{high} and y_{low}, respectively. Due to the asymmetric configuration, the interference fringes along *x* and *y* axis show different coupling phases. **e-g**, Diagrams of spin configurations of the condensations *x*, y_{high} and y_{low}, corresponding to the real-spaces of (**b**), (**c**), and (**d**), respectively. Each condensation has one ferromagnetic (blue dash lines) and one anti-ferromagnetic (solid blue lines) coupling with its nearest neighbors, showing a 90° compass model. Scale bars in (**b**), (**c**), and (**d**): 2 μm.
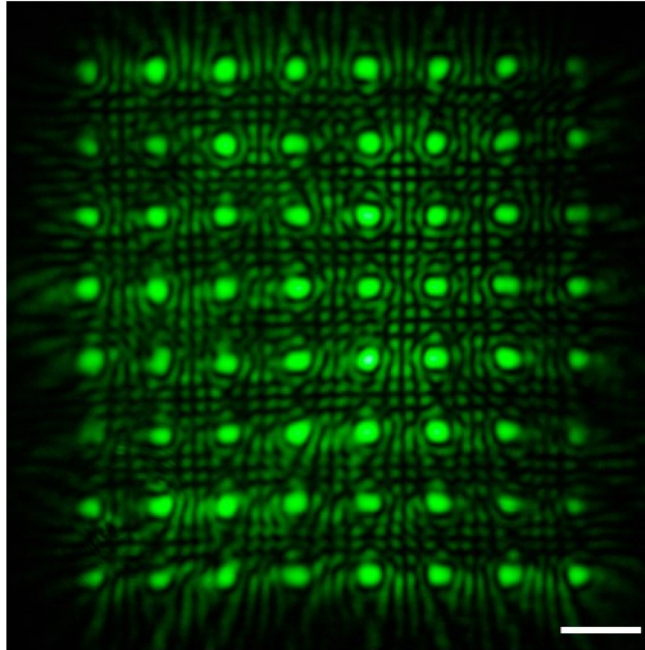
Supplementary Fig. 26 | A extended 8×8 polariton square lattice with anti-ferromagnetic coupling. The even interference fringes can be clearly identified. Scale bars: 5 μm.
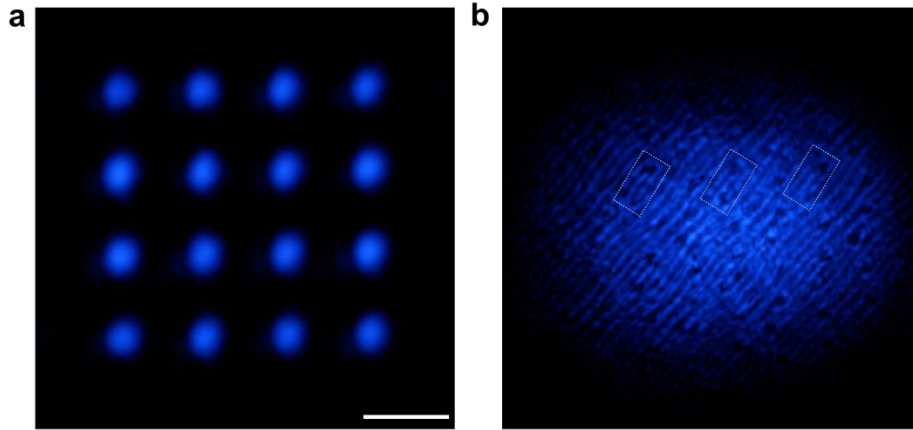
Supplementary Fig. 27 | Real-space (**a**) and k-space (**b**) images of a typical 4×4 laser dot array pattern generated by the spatial light modulator. A Gaussian-like pumping beam was reflected and modulated by a phase-only spatial light modulator to generate a laser dot array pattern. Thus, the k-space image of the laser spot pattern shows the periodic phase hologram superimposed with a Gaussian-like laser spot, as the marked white dotted frames in **b**. Scale bars in **a**: 5 μm.

References

1. Terças, H., Flayac, H., Solnyshkov, D. D. & Malpuech, G. Non-Abelian gauge fields in photonic cavities and photonic superfluids. *Phys. Rev. Lett.* **112**, 1–5 (2014).

2. Gianfrate, A. *et al.* Measurement of the quantum geometric tensor and of the anomalous Hall drift. *Nature* **578**, 381–385 (2020).

3. Ren, X. *et al.* Modulating crystal grain size and optoelectronic properties of perovskite films for solar cells by reaction temperature. *Nanoscale* **8**, 3816–3822 (2016).

4. Bao, W. *et al.* Observation of Rydberg exciton polaritons and their condensate in a perovskite cavity. *Proc. Natl. Acad. Sci. U. S. A.* **116**, 20274–20279 (2019).

5. Dirin, D. N., Cherniukh, I., Yakunin, S., Shynkarenko, Y. & Kovalenko, M. V. Solution-Grown CsPbBr3Perovskite Single Crystals for Photon Detection. *Chem. Mater.* **28**, 8470–8474 (2016).

6. Wouters, M., Carusotto, I. & Ciuti, C. Spatial and spectral shape of inhomogeneous nonequilibrium exciton-polariton condensates. *Phys. Rev. B* **77**, 115340 (2008).

7. Kalinin, K. P., Lagoudakis, P. G. & Berloff, N. G. Matter wave coupling of spatially separated and unequally pumped polariton condensates. *Phys. Rev. B* **97**, 094512 (2018).

8. Johnston, A., Kalinin, K. P. & Berloff, N. G. Artificial polariton molecules. *Phys. Rev. B* **103**, L060507 (2021).